

P1AC: Revisiting Absolute Pose From a Single Affine Correspondence

Jonathan Ventura

Department of Computer Science & Software Engineering
California Polytechnic State University

Zuzana Kukelova

Visual Recognition Group, Faculty of Electrical Engineering
Czech Technical University in Prague

Torsten Sattler

Visual Recognition Group, Faculty of Electrical Engineering
Czech Technical University in Prague

Dániel Baráth

Department of Computer Science
ETH Zürich

arXiv:2011.08790v2 [cs.CV] 17 Nov 2022

Abstract

Affine correspondences have traditionally been used to improve feature matching over wide baselines. While recent work has successfully used affine correspondences to solve various relative camera pose estimation problems, less attention has been given to their use in absolute pose estimation. We introduce the first general solution to the problem of estimating the pose of a calibrated camera given a single observation of an oriented point and an affine correspondence. The advantage of our approach (P1AC) is that it requires only a single correspondence, in comparison to the traditional point-based approach (P3P), significantly reducing the combinatorics in robust estimation. P1AC provides a general solution that removes restrictive assumptions made in prior work and is applicable to large-scale image-based localization. We propose two parameterizations of the P1AC problem and evaluate our novel solvers on synthetic data showing their numerical stability and performance under various types of noise. On standard image-based localization benchmarks we show that P1AC achieves more accurate results than the widely used P3P algorithm.

1 Introduction

Image-based localization is the process of determining the pose of a query image in a reference coordinate system from pre-registered images in a database. Image-based localization is an important technology for many applications including robotics [42], self-driving cars [19] and augmented reality [52]. It also forms an essential component of large-scale structure-from-motion pipelines [49].

The dominant method for image-based localization is to estimate the camera pose from correspondences between 2D features in the query image and known 3D points in the scene. Since these correspondences are likely to contain mismatches, a best-fit model is found through Random Sample Consensus (RANSAC) [16] or one of its derivatives [12, 33, 4], where camera pose hypotheses are estimated from minimal samples of three point correspondences

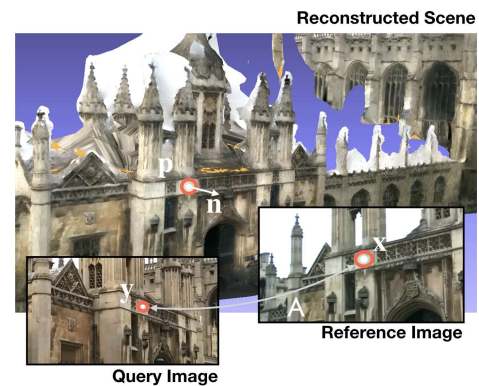


Figure 1: Overview of the P1AC problem. Our goal is to estimate the pose of a query image based on a single 2D observation of a known 3D oriented point in the scene and an affine correspondence to a reference image with known pose.

using a perspective-three-point (P3P) algorithm [16, 45].

In cases of very wide-baseline matching or extreme differences in viewing angle, affine-covariant features increase match reliability in comparison to traditional difference-of-Gaussian detectors such as SIFT [35]. A match between affine-covariant features, which we will call an affine correspondence (AC), estimates a 2×2 affine transformation matrix between the local regions around the corresponding points in the two images.

Recently, several authors have developed a theory of the constraints induced by ACs on two-view geometry [8, 46, 15], and minimal solvers for relative pose estimation from ACs [15, 14]. However, relatively little attention has been given to absolute pose computation from ACs. We revisit the topic of absolute pose computation from a single AC [29, 21]. In this work, we remove limiting assumptions made in previous work and propose the first general solution for absolute pose from a single AC. We call the problem of estimating camera pose from a single affine correspondence the perspective-one-affine-correspondence (P1AC) problem. In comparison to P3P solutions, our P1AC solutions only require

a single correspondence instead of three in the minimal case, and thus significantly reduces the complexity of robust estimation. We demonstrate these advantages through experiments on synthetic and real data.

Previous work has considered limited forms of the P1AC problem, by either assuming that the reference view is orthorectified [29], or that the query view uses a scaled orthographic projection [21]. In contrast, our method removes the limiting assumptions made in previous work and makes more general assumptions: that the reference and query images are perspective images of a locally planar surface in an arbitrary orientation, that we have estimated the normal of the observed 3D point, and that we have estimated an affine transformation between the reference and the query images.

Our contributions are as follows:

- We introduce three novel solutions to the P1AC problem: two solutions using Gröbner bases, and a faster solution using a reduction to the 3Q3 problem [30].
- Our solutions are general and do not impose the restrictive assumptions made in previous work.
- Experiments on synthetic data establish the numerical stability of our solvers and analyze their performance under various types of noise.
- Experiments on two benchmark datasets for image-based localization show that our P1AC solution produces more accurate pose estimates than P3P.

2 Related work

Affine correspondences are commonly estimated using either frame-to-frame tracking techniques [36, 2] or affine-covariant region detection [37, 39]. In the case of frame-to-frame tracking, the deformation of a locally planar surface observed by a moving camera is well-modeled by an affine transformation. For affine-covariant regions, an affine transformation describing the shape of the local region around the interest point is estimated [7]. The affine transformation between two regions A_i, A_j is then found as $A_j A_i^{-1}$. Even though affine-covariant regions increase the computational time required for feature detection, they have many advantages. ACs improve match reliability in wide-baseline image matching and they introduce new constraints on camera geometry and therefore they decrease the number of correspondences needed for camera pose estimation. Moreover, recently it was shown that convolutional neural networks can be used to reliably and quickly detect high-quality affine-covariant regions [40].

Given that affine transformations are estimated during the feature matching stage, recent work has examined how these transformations might be used to improve and simplify pose estimation and subsequently improve image-based localization, visual odometry, and structure-from-motion. Köser developed a theory of relationship between homographies and ACs [28], and Bentolila and Francos demonstrated that an AC provides three constraints on the fundamental matrix [8]. Raposo and Barreto re-derived these constraints [46], making them usable for essential matrix estimation using only two ACs instead of five PCs as is normally needed [43]. Eichhardt and Chetverikov extended relative pose estimation using ACs to handle any central camera model [15]. Eichhardt and Barath [14] demonstrated relative pose estimation from a single AC and a depth map estimated by a neural network. Recently, Barath

et al. provided recommendations for speeding up RANSAC when using ACs [5], including local feature geometry refinement and uncertainty propagation in RANSAC. The ideas presented in [5] can be used in combination with any pose estimation solver that uses affine correspondences, including the solvers proposed in this paper.

Absolute pose estimation using ACs has received much less attention than relative pose. Algorithms for absolute pose estimation from PCs has a long history, dating back to Grunert’s solution [17]. Among many recent P3P solutions [27, 25, 45] the state-of-the-art Lambda Twist method is the fastest while also being numerically stable [45].

Collins and Bartoli [13] derived novel constraints and a minimal solution for the absolute pose of a camera given a single 2D-3D correspondence and the homography between the object plane and the query image. In our case, we assume the surface is locally planar but we do not have access to a homography between the object plane and the query image. Instead, we are given an affine transformation between a reference image and the query image.

Köser and Koch introduced a solution for absolute pose from a single AC, with the restriction that the reference image is a scaled orthographic image of a planar surface with the surface normal parallel to the optical axis [29]. In our setting, the reference image is instead a perspective image of a locally planar surface in an arbitrary orientation. Their method could be applied in our setting if we rectified the image and then re-computed the affine region in the rectified image; however, this would be expensive as it would need to be done per-feature.

Haug and Jähne developed a solution for absolute pose from a single AC which allows for an arbitrary normal vector [21]. However, they apply a scaled orthographic projection assumption to the affine region in both the reference and query images, which makes the method less accurate when viewing the surface at wider angles. Our method does not make a scaled orthographic assumption and thus is not affected by the viewing angle to the surface.

3 Minimal solvers

Notation: We use a sans-serif capital letter M for a matrix, a bold lower-case letter \mathbf{v} for a vector, and an italic lower-case letter s for a scalar. We use subscripts to denote the rows of a matrix (\mathbf{r}_1 is the first row of matrix R) and the dimensions of a vector (p_1 is the first element of \mathbf{p}). A tilde over a vector indicates a homogeneous version of that vector ($\tilde{\mathbf{x}} = [x_1 \ x_2 \ 1]^T$). A bar over a matrix (\bar{P}) denotes the matrix P rearranged into a vector.

Consider two calibrated pinhole cameras observing a scene. We call the first camera the reference camera and the second one the query camera. We assume that the pose of the reference camera w.r.t. the world coordinate system is known. Without loss of generality we can assume that the reference camera has extrinsics $[1 \ | \ \mathbf{0}]^1$, and the query camera has extrinsics $[R \ | \ \mathbf{t}]$. Here R and \mathbf{t} represent the world-to-camera transformation, transforming points from the world coordinate system to the coordinate system of the query camera. This is a standard setup in localization pipelines, where our goal is to estimate the 3D rotation R and translation \mathbf{t} of the query camera.

¹In the general case, where the reference camera is not at the origin, we first transform the world coordinate system to place the reference camera at the origin and then apply the inverse transform to the resulting solution for R and \mathbf{t} .

The inputs to the PIAC are: corresponding points \mathbf{x} and \mathbf{y} in the reference and query image, respectively; A , the affine transformation from the local region around \mathbf{x} to the local region around \mathbf{y} ; d , the depth of the observed 3D point in the reference image; and \mathbf{n} , the surface normal at the 3D point in the coordinate system of the reference image.

First, we will develop a system of constraints on the pose of the query camera induced by the AC, and then we will describe solutions to two different parameterizations of this system.

3.1 Constraints induced by AC on camera pose

Let us define a function $f: \mathbb{R}^2 \rightarrow \mathbb{R}^2$ that maps points in the first image to points in the second one. Let \mathbf{x}, \mathbf{y} be corresponding points in the two images such that $\mathbf{y} = f(\mathbf{x})$. The first-order Taylor-approximation of f centered at \mathbf{x} is $\hat{f}(\mathbf{u}) = \mathbf{y} + A(\mathbf{u} - \mathbf{x})$, where $A = \nabla f(\mathbf{x})$ is the local affine transformation matrix.

Let $\pi^{-1}: \mathbb{R}^2 \rightarrow \mathbb{R}^3$ be the mapping from a point in the first image to the local 3D surface. Then we have

$$f(\mathbf{u}) = \pi(R\pi^{-1}(\mathbf{u}) + \mathbf{t}). \quad (1)$$

The projection function $\pi(\mathbf{p})$ is straightforward: $\pi(\mathbf{p}) = [p_1/p_3, p_2/p_3]^T$. The un-projection function $\pi^{-1}(\mathbf{u})$, however, requires knowledge of the scene geometry. We assume that the cameras observe a locally planar surface defined by 3D point $\mathbf{p} = d\tilde{\mathbf{x}}$ and normal \mathbf{n} such that \mathbf{p} projects to \mathbf{x} and \mathbf{y} in the first and second cameras, respectively. Let $\mathbf{u} = \mathbf{x} + \mathbf{z}$ be a point in the neighborhood of \mathbf{x} . To find $\pi^{-1}(\mathbf{u})$, we intersect ray \mathbf{u} with the plane to determine its corresponding 3D point. The plane is defined by

$$\mathbf{n}^T(\mathbf{p}' - \mathbf{p}) = 0, \quad (2)$$

where \mathbf{p}' is a point on the planar surface. Parameterizing the ray-plane intersection by $\mathbf{p}' = \alpha\tilde{\mathbf{u}}$, we have

$$\mathbf{n}^T(\alpha\tilde{\mathbf{u}} - \mathbf{p}) = 0, \quad (3)$$

thus resulting in

$$\alpha = \frac{\mathbf{n}^T\mathbf{p}}{\mathbf{n}^T\tilde{\mathbf{u}}}. \quad (4)$$

Therefore, under the assumption of a locally planar surface, we have determined $\pi^{-1}(\mathbf{u})$ as follows:

$$\pi^{-1}(\mathbf{u}) = \frac{\mathbf{n}^T\mathbf{p}}{\mathbf{n}^T\tilde{\mathbf{u}}}\tilde{\mathbf{u}}. \quad (5)$$

Let $\mathbf{q} = R\pi^{-1}(\mathbf{u}) + \mathbf{t}$. To compute $\nabla_{\mathbf{z}}f(\mathbf{u})$, we first apply the quotient rule to the Jacobian of the projection function $f(\mathbf{u}) = \pi(\mathbf{q})$ as follows:

$$\begin{aligned} \nabla_{\mathbf{z}}f(\mathbf{u}) &= \nabla_{\mathbf{z}}\pi(\mathbf{q}) = \nabla_{\mathbf{z}}\left(\frac{1}{q_3}\begin{bmatrix} q_1 \\ q_2 \end{bmatrix}\right) \\ &= \frac{1}{q_3^2}\left[q_3\left(\nabla_{\mathbf{z}}\begin{bmatrix} q_1 \\ q_2 \end{bmatrix}\right) - \begin{bmatrix} q_1 \\ q_2 \end{bmatrix}(\nabla_{\mathbf{z}}q_3)\right] \\ &= \frac{1}{q_3}\left[\nabla_{\mathbf{z}}\begin{bmatrix} q_1 \\ q_2 \end{bmatrix} - \frac{1}{q_3}\begin{bmatrix} q_1 \\ q_2 \end{bmatrix}(\nabla_{\mathbf{z}}q_3)\right] \end{aligned} \quad (6)$$

To make the expression linear in R, \mathbf{t} and simplify the later solution of the system of equations, we apply the substitution $\mathbf{v} = \frac{1}{q_3}[q_1 \quad q_2]^T$ to obtain

$$\nabla_{\mathbf{z}}f(\mathbf{u}) = \frac{1}{q_3}\left(\nabla_{\mathbf{z}}\begin{bmatrix} q_1 \\ q_2 \end{bmatrix} - \mathbf{v}(\nabla_{\mathbf{z}}q_3)\right). \quad (7)$$

Evaluating this expression at $\mathbf{z} = \mathbf{0}$ we obtain a final formula for $J = \nabla_{\mathbf{z}}f(\mathbf{u})|_{\mathbf{z}=\mathbf{0}}$ as follows:

$$J = \frac{1}{m}\left[d(\mathbf{n}^T\tilde{\mathbf{x}})(R_{1:2,1:2} - \mathbf{y}R_{3,1:2}) + (\mathbf{t}_{1:2} - t_3\mathbf{y})\mathbf{n}_{1:2}^T\right] \quad (8)$$

where $m = \mathbf{n}^T\tilde{\mathbf{x}}(d(\mathbf{r}_3\tilde{\mathbf{x}}) + t_3)$.

We multiply m on both sides of the constraint $A = J$ to cancel out the denominator and make the constraint linear. Our set of constraints to be solved is thus

$$y_1(\mathbf{r}_3\mathbf{p} + t_3) - (\mathbf{r}_1\mathbf{p} + t_1) = 0, \quad (9)$$

$$y_2(\mathbf{r}_3\mathbf{p} + t_3) - (\mathbf{r}_2\mathbf{p} + t_2) = 0, \quad (10)$$

$$ma_{11} - mj_{11} = 0, \quad ma_{12} - mj_{12} = 0, \quad (11)$$

$$ma_{21} - mj_{21} = 0, \quad ma_{22} - mj_{22} = 0, \quad (12)$$

where the first two constraints enforce that the 3D point projects to the 2D observation in the query camera, and the remaining constraints that the affine transformation matrix equals the Jacobian matrix derived above. Note that the only unknowns in equations 8 and 9-12 are elements of R and \mathbf{t} .

3.2 Minimal solutions

We have six independent constraints on the entries of R and \mathbf{t} and six degrees of freedom (three for the rotation and three for the translation). Therefore, we can solve for the absolute pose with a single AC.

3.2.1 Nullspace solution

If we parameterize the rotation directly as a 3×3 matrix, then we have 12 parameters in $P = [R \mid \mathbf{t}]$. We can write the six equations 9-12 as a matrix-vector multiply:

$$M\bar{\mathbf{P}} = \mathbf{0}. \quad (13)$$

Let B be the 12×6 nullspace of M . We compute the nullspace of M using singular value decomposition (SVD). Any solution, up to scale, for $\bar{\mathbf{P}}$ has the form

$$\bar{\mathbf{P}} = B\mathbf{b}, \quad (14)$$

where \mathbf{b} is a vector of six coefficients for the basis vectors in B . Our goal is to find solutions for \mathbf{b} that make the rotation matrix orthogonal.

We follow the solution procedure described by Ventura et al. [53]. Assuming $b_6 \neq 0$, we remove one parameter and simplify the solution by fixing $b_6 = 1$. Let $\mathbf{r}_1, \mathbf{r}_2, \mathbf{r}_3$ be the rows of R and $\mathbf{c}_1, \mathbf{c}_2, \mathbf{c}_3$ be the columns. The following constraints ensure that R is orthogonal, up to scale:

$$\begin{aligned} \|\mathbf{r}_1\|^2 - \|\mathbf{r}_2\|^2 &= 0, & \|\mathbf{r}_1\|^2 - \|\mathbf{r}_3\|^2 &= 0, \\ \|\mathbf{c}_1\|^2 - \|\mathbf{c}_2\|^2 &= 0, & \|\mathbf{c}_1\|^2 - \|\mathbf{c}_3\|^2 &= 0, \\ \mathbf{r}_1 \cdot \mathbf{r}_2 &= 0, & \mathbf{r}_1 \cdot \mathbf{r}_3 &= 0, & \mathbf{r}_2 \cdot \mathbf{r}_3 &= 0, \\ \mathbf{c}_1 \cdot \mathbf{c}_2 &= 0, & \mathbf{c}_1 \cdot \mathbf{c}_3 &= 0, & \mathbf{c}_2 \cdot \mathbf{c}_3 &= 0. \end{aligned} \quad (15)$$

Plugging in equation 14 to these constraints results in a system of ten quadratic equations in twenty-one monomials with variables b_1, \dots, b_5 . After extracting the roots of this system of equations, for each solution we divide $\bar{\mathbf{P}}$ by $\|\mathbf{c}_1\|$ and negate $\bar{\mathbf{P}}$ if necessary to ensure that $\det(R) = 1$.

This system has eight solutions and can be solved using the action matrix method and an automatic solver generator [32]. The resulting solver involves elimination of a 47×55 template matrix and eigendecomposition of an 8×8 matrix.

In contrast to [53], we discovered that the system of equations 15 can be further simplified by eliminating one unknown, e.g., b_1 . This can be done by rewriting the ten equations (15) in a matrix form $C\mathbf{v} = \mathbf{0}$, where C is a 10×21 coefficient matrix, and \mathbf{v} is a vector of 21 monomials ordered using the lexicographic ordering. After eliminating the matrix C , six monomials containing b_1 can be expressed as quadratic polynomials in b_2, \dots, b_5 . In this way, b_1 can be eliminated from the original equations. Moreover, new equations that express relationships between different monomials can be added to the original equations, e.g. if $b_1 = p_1(b_2, \dots, b_5)$ and $b_1 b_2 = p_2(b_2, \dots, b_5)$, where p_1 and p_2 are polynomials in b_2, \dots, b_5 , extracted from the eliminated matrix C , then a new equation that can be added to the original equations has the form $p_1 b_2 = p_2$. In this way, a new system of polynomial equations in four unknowns can be generated. This system can be solved using the automatic generator [32] and results in a solver that performs elimination of a 29×37 template matrix and eigendecomposition of an 8×8 matrix.

3.2.2 3Q3 solution

A faster and more stable solution is obtained using the Cayley parameterization of the rotation with parameters x, y, z :

$$R = \frac{1}{s} \begin{bmatrix} 1+x^2-y^2-z^2 & 2(xy-z) & 2(y+xz) \\ 2(xy+z) & 1-x^2+y^2-z^2 & 2(yz-x) \\ 2(xz-y) & 2(x+yz) & 1-x^2-y^2+z^2 \end{bmatrix} \quad (16)$$

where $s = 1 + x^2 + y^2 + z^2$. Note that we cannot represent 180° rotations with this parameterization; however, this degenerate configuration is not a problem in practice since it would mean that the reference and the query camera have no visual overlap.

After plugging this parameterization of R into equations 9–12, we multiply all equations by s to cancel out the denominator in R .

Let $\mathbf{p} = [st_1, st_2, st_3, x^2, xy, xz, y^2, yz, z^2, x, y, z, 1]^T$. Writing the equations 9–12 as a matrix-vector multiplication $M\mathbf{p} = \mathbf{0}$, we first eliminate \mathbf{st} using Gauss-Jordan elimination. This leaves three quadratic equations in ten monomials on x, y, z – a 3Q3 problem. Kukulova et al. [30] introduced a fast solver for the 3Q3 problem which produces up to eight solutions for x, y, z . We use the implementation by Larsson² which uses several techniques to improve the stability of the original solver [57]. Once we obtain solutions for x, y, z , we solve for \mathbf{t} by backsubstitution into equations 9–12.

4 Evaluation

We performed evaluations on synthetic and real data to test the numerical stability of our solvers, test robustness to various types of noise, and assess their performance as part of a image-based localization system.

We compared the following algorithms in our evaluation:

- **P3P** Standard P3P absolute pose calculation from three 2D-3D point observations. We used the state-of-the-art Lambda Twist P3P solver [45].

²<https://github.com/vlarsson/re3q3>

- **P1AC (Null)** Our solver using the nullspace solution with reduction to a 47×55 elimination template (Section 3.2.1).
- **P1AC (Elim)** Our solver using the nullspace solution and elimination of an additional unknown, with reduction to a 29×37 elimination template (Section 3.2.1).
- **P1AC (3Q3)** Our solver using the Cayley rotation parameterization and the 3Q3 solver (Section 3.2.2).

In our evaluations we computed two pose accuracy metrics. Given the true camera rotation R and the estimated camera rotation \hat{R} we computed the *rotation error* as $|\ln(\hat{R}R^T)|$, where $\ln(\cdot)$ denotes the $SO(3)$ logarithm [22, 20]. Given the true camera center \mathbf{c} and the estimated camera center $\hat{\mathbf{c}}$, we computed the *position error* as $\|\mathbf{c} - \hat{\mathbf{c}}\|$. When considering multiple solutions produced by a method, we choose the solution that minimizes the maximum of these two error metrics.

4.1 Synthetic data experiments

We generated synthetic problem instances with varying levels of noise added to the 2D point observations, affine transformations, and normal vectors.

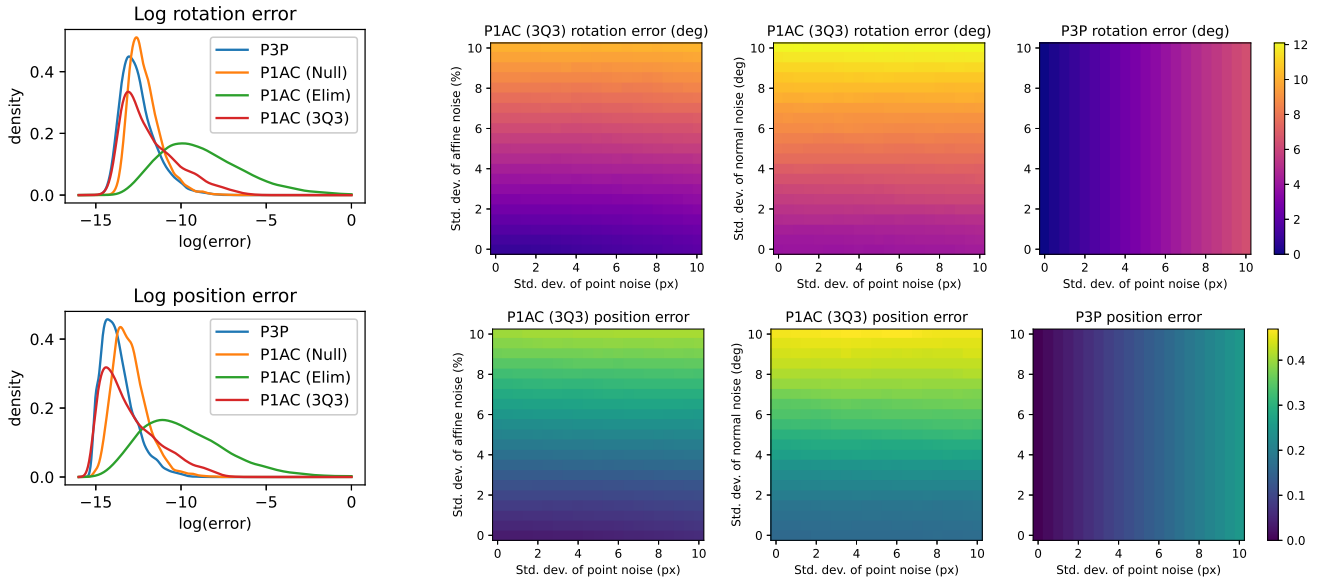
We generated synthetic random problems in the following manner adapted from [14]. We randomly place two cameras around the origin at a distance sampled from $[1, 2]$, both oriented towards a random target point sampled from $[-0.5, 0.5]^3$. To generate a correspondence between the two cameras, we select a random 3D point from $\mathbb{N}(\mathbf{0}, I_{3 \times 3})$ with a random normal vector. We project the 3D point to the two cameras using a focal length of 400. We then calculate the affine transformation from the local homography between the first and second cameras [3]. We transform the cameras and 3D points so that the first camera (the reference camera) is at the origin with identity rotation.

We add Gaussian noise to the 2D point observations directly. Following prior studies [15, 14] we add Gaussian noise directly to the elements of the 2×2 affine transformation matrix. We select the level of affine noise according to the chosen percentage error; i.e., if the chosen percentage error is e , the std. dev. of the noise added to a_{ij} is $e \cdot a_{ij}$. Finally, we add noise to the normal vectors by rotating them by a random rotation whose angle is randomly chosen from a Gaussian distribution. For each problem instance, we generate three correspondences between the two cameras, so that we can test both P1AC (using the first correspondence) and P3P (using all three correspondences) on the same problem instance.

Numerical stability To evaluate the numerical stability of each solver, we computed the rotation and position errors of each solver over 10,000 random problem instances with zero noise added. Figure 2a shows the results. P3P, P1AC (Null), and P1AC (3Q3) all have similar performance, with P1AC (3Q3) having the lowest median error for both metrics. P1AC (Elim) exhibited generally higher error than the other solvers, although the median log error is still below -10 in both metrics. Overall, all solvers exhibited good stability without large errors.

Timings We computed the average timing of the solvers over 10,000 random problem instances. The solvers were implemented in C++ and timings were made on an Apple M1 Pro CPU. We used the implementations of Lambda Twist and 3Q3 provided in PoseLib [31]. The results are given in Table 1.

Among our P1AC solutions, P1AC (3Q3) is by far the fastest with an average timing of $2.59 \mu\text{s}$. The P3P solver is about $6 \times$



(a) Numerical stability

(b) Noise

Figure 2: Results of synthetic data experiments. (a) Analysis of numerical stability with zero noise added to observations. The plots are estimates of the distribution produced by Gaussian kernel-density estimation. *Top*: Log rotation error; *Bottom*: Log position error. (b) Analysis of error with respect to various types and levels of noise. *Left*: Error of P1AC (3Q3) solver w.r.t. affine and point noise, with normal noise fixed to 1° . *Center*: Error of P1AC (3Q3) solver w.r.t. normal and point noise, with affine noise fixed to 4%. *Right*: Error of P3P solver w.r.t. affine and point noise. (The P3P solver does not use the affine transformation and thus is unaffected by affine noise.)

	P3P [45]	P1AC		
		Null	Elim	3Q3
Time (μs)	0.39	26.60	16.71	2.59

Table 1: Average timing in μs over 10,000 trials.

faster than P1AC (3Q3). The Lambda Twist solver is based on a careful elimination of the rotation and translation parameters to reveal the underlying elliptic equations in the P3P problem which are solved through diagonalization. Since the Null solver and its Elim variant involve iterative methods such as SVD and eigendecomposition they are far slower than the P3P solver. The 3Q3 version is faster than Null and Elim for many reasons: it solves a simpler system than the nullspace parameterization (involving fewer unknowns); it is carefully designed using manual tricks to directly derive a polynomial in one variable; it does not need to use SVD; and it uses Sturm sequences instead of eigendecomposition to solve for the polynomial roots.

Noise Since P1AC (3Q3) was the fastest among our P1AC solutions and had good numerical stability, we only use that version of our solver in our noise tests and real data tests (Section 4.2). We tested the P1AC (3Q3) solver and the P3P solver over a range of noise levels in the 2D point observations, affine transformation matrices, and normal vectors. We tested 1000 random problem instances for each setting of the noise levels. Figure 2b plots the median errors for each method at each setting.

The left column of Figure 2b presents the results for increasing levels of point and affine noise, with the std. dev. of the normal vector noise set to 1 degree. We increased the std. dev. of 2D observation noise from 0 to 10 pixels and the std. dev. of affine noise from 0 to 10%. This is the same range of affine noise used in

[14].

The center column of Figure 2b presents the results for increasing levels of point and normal vector noise, with the std. dev. of the affine noise set to 4%, which was identified as a realistic level of affine noise in [14]. We increased the std. dev. of 2D observation noise from 0 to 10 pixels and the std. dev. of the normal vector noise from 0° to 10° .

The right column of Figure 2b presents the results for the P3P solver, for comparison. The P3P solver does not use the affine transformation or normal vector and thus is unaffected by affine and normal noise.

The synthetic experiments show that the P1AC solver is affected by affine and normal noise much more than by 2D point observation noise. In the presence of affine and normal noise, it returns larger errors than the P3P solver, which is not affected by these noises. Nevertheless, for noise levels that correspond to realistic values, i.e. 2%-4% for affine noise and 1° for normal noise, the P1AC solver still returns reasonably small errors that are sufficient for the initialization of local optimization inside RANSAC.

4.2 Real data experiments

In the real data experiments, we only tested the P1AC (3Q3) version of our solvers, and in this subsection we refer to it as P1AC. To evaluate the performance of our method for large-scale image-based localization, we used the Cambridge Landmarks [26] and Aachen Day-Night v1.1 from [48, 47, 56] benchmark datasets. Both datasets are commonly used in the visual localization literature.

The Cambridge Landmarks dataset consists of six scenes, each recorded through multiple video sequences taken by a mobile phone, depicting parts of Cambridge, UK. Out of the sequences

Scene	# Frames		Position (cm) ↓		Rotation (°) ↓		Recall (0.1m/1°) ↑		Recall (0.2m/1°) ↑	
	Train	Test	P3P	P1AC	P3P	P1AC	P3P	P1AC	P3P	P1AC
Great Court	1535	760	8	6	0.10	0.08	61.8	73.6	86.4	91.1
King’s College	1220	343	10	7	0.16	0.14	49.3	64.7	79.3	86.9
Old Hospital	895	182	9	7	0.15	0.11	58.8	72.5	79.7	93.4
Shop Facade	231	103	4	3	0.13	0.13	85.4	87.4	94.2	95.1
St Mary’s Church	1487	530	7	5	0.21	0.17	61.7	72.5	80.9	87.7
Street	3015	2923	32	20	0.57	0.35	10.7	19.8	18.0	29.7
All			12	8	0.22	0.16	54.6	65.1	73.1	80.7

Table 2: **Cambridge Landmarks** [26] median position (centimeters) and rotation (degrees) errors, and recalls (percentages), at 0.1m/1° and 0.2m/1°, of GC-RANSAC [4] combined with P3P and the proposed P1AC (3Q3) solver. The average over all scenes is in the last row.

	Recall (0.25m/2°) ↑		Recall (0.5m/5°) ↑		Recall (5m/10°) ↑	
	P3P	P1AC	P3P	P1AC	P3P	P1AC
Day	61.3	61.9	83.4	84.0	95.1	95.6
Night	16.3	17.3	32.7	34.7	74.4	83.7

Table 3: **Aachen Day-Night** pose error recalls [48], in percentages, at 0.25m/2°, 0.5m/5°, and 5.0m/10° of GC-RANSAC [4] combined with P3P and the proposed P1AC (3Q3) minimal solver.

recorded for each dataset, some are used to obtain database images that represent the scene while the others are used to obtain query images. Ground truth poses and intrinsic camera calibrations for all images were obtained using the VisualSFM [54, 55] Structure-from-Motion (SfM) software. Visual localization performance is typically measured by reporting the median position and orientation error. In addition, we measure the percentage of images localized within 10cm and 1° respectively 20cm and 1° of their ground truth poses.

The Cambridge Landmarks is a relatively easy dataset since each scene is rather small and the query images were taken around the same time as the database images. A much more challenging case is the Aachen Day-Night dataset, which depicts the historical inner city of Aachen, Germany. The database images were all taken during daytime conditions and the dataset provides query images taken at nighttime conditions over a longer period of time. Ground truth for the database images were obtained via COLMAP [49]. The nighttime queries were later registered by refining initial pose estimates [56]. We follow the common evaluation protocol and report the percentage of images localized within three error thresholds (0.25m/2°, 0.5m/5°, 5m,10°).

There are multiple ways to obtain affine features from real images. The most standard is to use a local feature detector, like DoG [35] or Key.Net [6], estimate keypoint locations and scales, and use the patch-based AffNet [39] to get affine shapes. Finally, a patch-based descriptor, like HardNet [38] or SOSNet [50], is applied. In our experiments, we run the DoG detector followed by AffNet to recover the affine shape of the features. Finally, HardNet extracts the descriptors on the affinely warped local patches. This approach is among the leaders in the IMC 2020 benchmark [23].

Finally, we apply the normal estimator implemented in MeshLab to obtain an oriented point cloud. The normals are fitted to the 200 nearest neighbors.

4.3 Image localization procedure

For both datasets, we use image retrieval to identify a small set of potentially relevant database images for each query photo. We use DenseVLAD [51] descriptors for Cambridge Landmarks and NetVLAD [1] descriptors for Aachen Day-Night. We then establish 2D-2D correspondences between each query and its retrieved database images. These 2D-2D matches are then lifted to 2D-3D correspondences. For Cambridge Landmarks, we use the 3D points in SfM point clouds corresponding to the features extracted from the database images. For Aachen, we use a dense depth maps obtained by rendering a mesh model of the scene to obtain the 3D points (and their corresponding normals) for the database features [44].

To estimate the pose of each query image, we iterate through the retrieved database images. Between each pair, we estimate the pose by Graph-Cut RANSAC [4] (GC-RANSAC) using the implementation provided by the authors. The final pose for a query image comes from the database image with which the highest inlier number is achieved. GC-RANSAC requires two types of solvers, one for minimal and one for non-minimal pose estimation. We test the proposed P1AC (3Q3) solver as the minimal solver and compare it to P3P solver [45]. The non-minimal solver, running both in the local optimization and in the final refitting on all inliers, is always EPnP [34] followed by a few iterations of the Levenberg-Marquardt optimization [41] minimizing the pose error. The proposed P1AC solver enables running GC-RANSAC exhaustively, without severely affecting the run-time. Therefore, we test the pose from all correspondences without using a random sampler. For P3P solver, we use the PROSAC sampler [11] on matches ordered by SNN ratio.

For Cambridge Landmarks, we set the inlier-outlier threshold to 4 pixels. For Aachen Day-Night, we set it to 12 pixels. We tuned the SNN ratio threshold for both P3P and P1AC. For P3P, 0.9 works the best. Surprisingly, P1AC is the most accurate on Cambridge Landmarks without any SNN ratio filtering. Even though this leads to slightly increased run-times due to running on much more points, it increases both the accuracy and inlier number significantly.

4.4 Pose accuracy

A summary of errors on the Cambridge Landmarks dataset is given in Table 2. We report the median position (in meters) and rotation errors (in degrees), and the recall (in percentages) at 0.1m/1° and

0.2m/1°. The proposed PIAC method has lower errors and thus, higher recall on *all* scenes. In many cases, the recall increase is significant. For example, on scene Street (i.e., the most challenging scene in the dataset) both recall values increase by around 10%. The average 0.1m/1° over all scenes is increased by 10.5% and the average 0.2m/1° by 7.6%.

The recalls at 0.25m/2°, 0.5m/5°, and 5.0m/10° on the Aachen Day-Night [48] dataset are reported in Table 3. In this case, both method uses an SNN ratio threshold set to 0.9 since increasing it led to a deterioration in the accuracy. This is likely caused by the dataset being more challenging than the Cambridge Landmarks. While the accuracy difference is smaller than in Table 2, the proposed PIAC consistently improves the results. On the Night sequence, the recall at 5.0m/10° is increased quite significantly by 9.3%.

Table 4 reports the average inlier numbers and processing times (in seconds). On Cambridge Landmarks, as expected from the increased SNN ratio threshold, the average inlier number returned by PIAC is significantly higher than that of P3P. This comes at the price of an increased run-time. On Aachen Day-Night, both methods use the same SNN ratio threshold and the proposed PIAC is faster on both scenes while leading to similar inlier numbers.

4.5 Affine to Point Conversion

We also evaluated a baseline method where we convert a single AC to three PCs. The AC already contains one 2D-3D PC. Two additional 2D-2D PCs are generated via the local affine frame in each image. The points in the database image are then projected into the 3D plane determined by the surface normal. These two intersections are the new 3D points forming the 2D-3D correspondences with the points in the query image. Note that this approach involves two approximations. Since the local affine frame is the first-order approximation of the imaging function, it holds only infinitely close to the observed location – thus, the generated PCs will only be approximations. Second, intersecting the rays from the database image with the plane implied by the normal is only correct if the observed 3D point actually lies on a 3D plane. Otherwise, the 3D points will be incorrect.

We tested this approach on Cambridge Landmarks. Despite the inherent approximations, it achieves 56.2% recall at 0.1m/1° and 75.2% at 0.2m/1°. This is more accurate than P3P (recall of 54.6% and 73.1%, respectively) but less accurate than the proposed PIAC solver (recall of 65.1% and 80.7%, respectively). The average run-time of this approach is 0.38 seconds which is similar to that of PIAC.

5 Discussion

In terms of timing, our PIAC solvers are slower than the P3P solver. However, the PIAC (3Q3) solver is still quite fast ($< 3\mu\text{s}$) and its computation time is negligible compared to other steps in the random sampling process such as local optimization and inlier testing.

Our real data experiment demonstrates the benefit of using our PIAC solvers in place of P3P in an image-based localization pipeline. PIAC achieves pose accuracy better than P3P while decreasing the total computation time in some cases.

Scene	Inliers \uparrow		Time (secs) \downarrow	
	P3P	PIAC	P3P	PIAC
Great Court	533	772	0.14	0.26
King’s College	2679	3306	0.19	0.48
Old Hospital	1064	1581	0.12	0.42
Shop Facade	1578	2157	0.13	0.37
St Mary’s Church	1211	1536	0.12	0.38
Street	209	390	0.10	0.24
Day	244	246	0.24	0.09
Night	56	52	0.12	0.09

Table 4: Avg. inlier numbers and run-times (secs) of GC-RANSAC [4] with P3P and the proposed PIAC (3Q3) solver on the Cambridge Landmarks [26] and Aachen Day-Night [48] datasets.

In comparison to the baseline method of applying P3P to point correspondences generated from a single AC, our PIAC (3Q3) method successfully localized more frames and was more accurate. This indicates that our approach based on differential analysis of the AC more accurately models the constraint imposed by an AC on the absolute pose of the query camera.

There are several approaches to improving the ACs and thus possibly increasing the accuracy of the PIAC result on challenging images. Improving the AC quality might also lead to a speed up in sample consensus because the initial pose estimates by the PIAC solver would be more accurate, and thus the system would spend less time during the local optimization steps. For example, Barath et al. [5] proposed an efficient technique called least squares matching (LSM) for symmetric affine correspondence refinement.

With other minimal solvers that use a single correspondence, histogram or kernel density voting [10] is often used in place of RANSAC. However, we did not find voting to be applicable here because we have a six DOF problem whereas voting is usually applied when estimating a single parameter such as the focal length [10, 18].

6 Conclusions and future work

In this work we derived novel constraints imposed by an affine correspondence on the absolute pose of a camera, given knowledge of a 3D point in the scene, the surface normal at that point, and the pose of the reference image. Using these novel constraints we developed three minimal solutions for absolute pose from a single AC. Through experiments on synthetic data we established the numerical stability of our solvers and their behavior under increasing levels of noise in the 2D point observation, affine transformation matrix, and normal vector. Finally, we demonstrated the usefulness of our solver in an image-based localization system. In our experiments, replacing P3P with our PIAC solvers improved localization accuracy and recall.

Future work lies in similarly applying constraints from ACs to uncalibrated absolute pose problems [9, 24].

Acknowledgments

This work was partially supported by National Science Foundation Award No. 2144822.

References

- [1] Relja Arandjelović, Petr Gronat, Akihiko Torii, Tomas Pajdla, and Josef Sivic. NetVLAD: CNN architecture for weakly supervised place recognition. In *CVPR*, 2016. 6
- [2] Simon Baker and Iain Matthews. Lucas-kanade 20 years on: A unifying framework. *International journal of computer vision*, 56(3):221–255, 2004. 2
- [3] Daniel Barath and Levente Hajder. Novel ways to estimate homography from local affine transformations. In *Proceedings of the International Joint Conference on Computer Vision, Imaging and Computer Graphics Theory and Applications*, pages 434–445, 2016. 4
- [4] Daniel Barath and Jiri Matas. Graph-cut RANSAC: local optimization on spatially coherent structures. *IEEE Transactions on Pattern Analysis and Machine Intelligence*, 44(9):4961–4974, 2021. 1, 6, 7
- [5] Daniel Barath, Michal Polic, Wolfgang Förstner, Torsten Sattler, Tomas Pajdla, and Zuzana Kukelova. Making affine correspondences work in camera geometry computation. In *European Conference on Computer Vision (ECCV)*, 2020. 2, 7
- [6] Axel Barroso-Laguna, Edgar Riba, Daniel Ponsa, and Krystian Mikolajczyk. Key.Net: Keypoint Detection by Handcrafted and Learned CNN Filters. In *ICCV*, 2019. 6
- [7] Adam Baumberg. Reliable feature matching across widely separated views. In *Proceedings IEEE Conference on Computer Vision and Pattern Recognition. CVPR 2000 (Cat. No. PR00662)*, volume 1, pages 774–781. IEEE, 2000. 2
- [8] Jacob Bentolila and Joseph M Francos. Conic epipolar constraints from affine correspondences. *Computer Vision and Image Understanding*, 122:105–114, 2014. 1, 2
- [9] Martin Bujnak, Zuzana Kukelova, and Tomas Pajdla. A general solution to the p4p problem for camera with unknown focal length. In *2008 IEEE Conference on Computer Vision and Pattern Recognition*, pages 1–8. IEEE, 2008. 7
- [10] Martin Bujnak, Zuzana Kukelova, and Tomas Pajdla. Robust focal length estimation by voting in multi-view scene reconstruction. In *Asian Conference on Computer Vision*, pages 13–24. Springer, 2009. 7
- [11] Ondrej Chum and Jiri Matas. Matching with PROSAC-progressive sample consensus. In *2005 IEEE computer society conference on computer vision and pattern recognition (CVPR'05)*, volume 1, pages 220–226. IEEE, 2005. 6
- [12] Ondřej Chum, Jiří Matas, and Josef Kittler. Locally optimized ransac. In *Joint Pattern Recognition Symposium*, pages 236–243. Springer, 2003. 1
- [13] Toby Collins and Adrien Bartoli. Infinitesimal plane-based pose estimation. *International journal of computer vision*, 109(3):252–286, 2014. 2
- [14] Ivan Eichhardt and Daniel Barath. Relative pose from deep learned depth and a single affine correspondence. In *European Conference on Computer Vision*, pages 627–644. Springer, 2020. 1, 2, 4, 5
- [15] Iván Eichhardt and Dmitry Chetverikov. Affine correspondences between central cameras for rapid relative pose estimation. In *Proceedings of the European Conference on Computer Vision (ECCV)*, pages 482–497, 2018. 1, 2, 4
- [16] Martin A Fischler and Robert C Bolles. Random sample consensus: a paradigm for model fitting with applications to image analysis and automated cartography. *Communications of the ACM*, 24(6):381–395, 1981. 1
- [17] J Grunert. Das pothenotische problem in erweiterter gestalt nebst über seine anwendungen in der geodäsie. *Grunerts archive für mathematik und physik*, 1:238–248, 1841. 2
- [18] Levente Hajder and Daniel Barath. Relative planar motion for vehicle-mounted cameras from a single affine correspondence. In *2020 IEEE International Conference on Robotics and Automation (ICRA)*, pages 8651–8657. IEEE, 2020. 7
- [19] Christian Häne, Lionel Heng, Gim Hee Lee, Friedrich Fraundorfer, Paul Furgale, Torsten Sattler, and Marc Pollefeys. 3d visual perception for self-driving cars using a multi-camera system: Calibration, mapping, localization, and obstacle detection. *Image and Vision Computing*, 68:14–27, 2017. 1
- [20] Richard Hartley, Jochen Trumpf, Yuchao Dai, and Hongdong Li. Rotation averaging. *International journal of computer vision*, 103(3):267–305, 2013. 4
- [21] Florian Haug and Bernd Jähne. 6 dof appearance-based object localization with local covariant features. *F. Puente León/M. Heizmann (Hrsg.)*, page 13, 2010. 1, 2
- [22] Du Q Huynh. Metrics for 3d rotations: Comparison and analysis. *Journal of Mathematical Imaging and Vision*, 35(2):155–164, 2009. 4
- [23] Yuhe Jin, Dmytro Mishkin, Anastasiia Mishchuk, Jiri Matas, Pascal Fua, Kwang Moo Yi, and Eduard Trulls. Image matching across wide baselines: From paper to practice. *International Journal of Computer Vision*, 2020. 6
- [24] Klas Josephson and Martin Byrod. Pose estimation with radial distortion and unknown focal length. In *2009 IEEE Conference on Computer Vision and Pattern Recognition*, pages 2419–2426. IEEE, 2009. 7
- [25] Tong Ke and Stergios I Roumeliotis. An efficient algebraic solution to the perspective-three-point problem. In *Proceedings of the IEEE Conference on Computer Vision and Pattern Recognition*, pages 7225–7233, 2017. 2
- [26] Alex Kendall, Matthew Grimes, and Roberto Cipolla. Posenet: A convolutional network for real-time 6-dof camera relocalization. In *Proceedings of the IEEE international conference on computer vision*, pages 2938–2946, 2015. 5, 6, 7
- [27] Laurent Kneip, Davide Scaramuzza, and Roland Siegwart. A novel parametrization of the perspective-three-point problem for a direct computation of absolute camera position and orientation. In *CVPR 2011*, pages 2969–2976. IEEE, 2011. 2
- [28] Kevin Köser. *Geometric estimation with local affine frames and free-form surfaces*. PhD thesis, University of Kiel, 2009. 2
- [29] Kevin Köser and Reinhard Koch. Differential spatial resection-pose estimation using a single local image feature. In *European Conference on Computer Vision*, pages 312–325. Springer, 2008. 1, 2
- [30] Zuzana Kukelova, Jan Heller, and Andrew Fitzgibbon. Efficient intersection of three quadrics and applications in computer vision. In *Proceedings of the IEEE Conference on Computer Vision and Pattern Recognition*, pages 1799–1808, 2016. 2, 4
- [31] Viktor Larsson. PoseLib - Minimal Solvers for Camera Pose Estimation, 2020. 4
- [32] Viktor Larsson, Kalle Astrom, and Magnus Oskarsson. Efficient solvers for minimal problems by syzygy-based reduction. In *Proceedings of the IEEE Conference on Computer Vision and Pattern Recognition*, pages 820–829, 2017. 4
- [33] Karel Lebeda, Jiri Matas, and Ondrej Chum. Fixing the Locally Optimized RANSAC. In *British Machine Vision Conference (BMVC)*, 2012. 1
- [34] Vincent Lepetit, Francesc Moreno-Noguer, and Pascal Fua. Epnp: An accurate $o(n)$ solution to the pnp problem. *International journal of computer vision*, 81(2):155, 2009. 6
- [35] David G Lowe. Distinctive image features from scale-invariant keypoints. *International journal of computer vision*, 60(2):91–110, 2004. 1, 6
- [36] Bruce D Lucas and Takeo Kanade. An iterative image registration technique with an application to stereo vision. *Proceedings DARPA image Understanding Workshop*, 1981. 2
- [37] Krystian Mikolajczyk and Cordelia Schmid. Scale & affine invariant interest point detectors. *International journal of computer vision*, 60(1):63–86, 2004. 2

- [38] A. Mishchuk, D. Mishkin, F. Radenovic, and J. Matas. Working Hard to Know Your Neighbor’s Margins: Local Descriptor Learning Loss. In *NeurIPS*, 2017. 6
- [39] D. Mishkin, F. Radenovic, and J. Matas. Repeatability is Not Enough: Learning Affine Regions via Discriminability. In *ECCV*, 2018. 2, 6
- [40] Dmytro Mishkin, Filip Radenovic, and Jiri Matas. Repeatability is not enough: Learning affine regions via discriminability. In *Proceedings of the European Conference on Computer Vision (ECCV)*, pages 284–300, 2018. 2
- [41] Jorge J Moré. The levenberg-marquardt algorithm: implementation and theory. In *Numerical analysis*, pages 105–116. Springer, 1978. 6
- [42] Raul Mur-Artal and Juan D Tardós. Orb-slam2: An open-source slam system for monocular, stereo, and rgb-d cameras. *IEEE transactions on robotics*, 33(5):1255–1262, 2017. 1
- [43] David Nistér. An efficient solution to the five-point relative pose problem. *IEEE transactions on pattern analysis and machine intelligence*, 26(6):756–770, 2004. 2
- [44] Vojtech Panek, Zuzana Kukelova, and Torsten Sattler. Meshloc: Mesh-based visual localization. In *ECCV*, 2022. 6
- [45] Mikael Persson and Klas Nordberg. Lambda Twist: An accurate fast robust perspective three point (p3p) solver. In *Proceedings of the European Conference on Computer Vision (ECCV)*, pages 318–332, 2018. 1, 2, 4, 5, 6
- [46] Carolina Raposo and Joao P Barreto. Theory and practice of structure-from-motion using affine correspondences. In *Proceedings of the IEEE Conference on Computer Vision and Pattern Recognition*, pages 5470–5478, 2016. 1, 2
- [47] Torsten Sattler, Will Maddern, Carl Toft, Akihiko Torii, Lars Hammarstrand, Erik Stenborg, Daniel Safari, Masatoshi Okutomi, Marc Pollefeys, Josef Sivic, Fredrik Kahl, and Tomas Pajdla. Benchmarking 6DOF Urban Visual Localization in Changing Conditions. In *CVPR*, 2018. 5
- [48] Torsten Sattler, Tobias Weyand, Bastian Leibe, and Leif Kobbelt. Image retrieval for image-based localization revisited. In *BMVC*, volume 1, page 4, 2012. 5, 6, 7
- [49] Johannes Lutz Schönberger and Jan-Michael Frahm. Structure-from-motion revisited. In *Conference on Computer Vision and Pattern Recognition (CVPR)*, 2016. 1, 6
- [50] Yurun Tian, Xin Yu, Bin Fan, Fuchao Wu, Huub Heijnen, and Vasileios Balntas. Sosnet: Second order similarity regularization for local descriptor learning. In *CVPR*, 2019. 6
- [51] Akihiko Torii, Relja Arandjelović, Josef Sivic, Masatoshi Okutomi, and Tomas Pajdla. 24/7 Place Recognition by View Synthesis. In *CVPR*, 2015. 6
- [52] Jonathan Ventura, Clemens Arth, Gerhard Reitmayr, and Dieter Schmalstieg. Global localization from monocular slam on a mobile phone. *IEEE transactions on visualization and computer graphics*, 20(4):531–539, 2014. 1
- [53] Jonathan Ventura, Clemens Arth, Gerhard Reitmayr, and Dieter Schmalstieg. A minimal solution to the generalized pose-and-scale problem. In *Proceedings of the IEEE Conference on Computer Vision and Pattern Recognition*, pages 422–429, 2014. 3, 4
- [54] Changchang Wu. Towards linear-time incremental structure from motion. In *2013 International Conference on 3D Vision-3DV 2013*, pages 127–134. IEEE, 2013. 6
- [55] Changchang Wu, Sameer Agarwal, Brian Curless, and Steven M Seitz. Multicore bundle adjustment. In *CVPR 2011*, pages 3057–3064. IEEE, 2011. 6
- [56] Zichao Zhang, Torsten Sattler, and Davide Scaramuzza. Reference Pose Generation for Long-term Visual Localization via Learned Features and View Synthesis. *IJCV*, 2020. 5, 6
- [57] Lipu Zhou, Jiamin Ye, and Michael Kaess. A stable algebraic camera pose estimation for minimal configurations of 2d/3d point and line correspondences. In *Asian Conference on Computer Vision*, pages 273–288. Springer, 2018. 4